Article

Miniaturized Head-Mount Doppler Optical Coherence Tomography Scope for Freely Moving Mouse

Jingyi Wang, Qiao Ye, Lidek Chou, Saijun Qiu, Xiangmin Xu, and Zhongping Chen*

Cite This: *ACS Photonics* 2024, 11, 3381−3389

Read Online

ACCESS | Metrics & More | Article Recommendations | Supporting Information

ABSTRACT: This study presents a miniaturized head-mount optical coherence tomography (OCT) system tailored for high-resolution brain imaging in freely moving mice, providing an advanced noninvasive imaging tool in neuroscience research. Leveraging optical coherence tomography technology, the system enables depth-resolved imaging and integrates functional OCT extensions, including angiography and Doppler imaging. Remarkably lightweight at 1.5 g, the device allows for the preservation of natural mouse behavior during imaging sessions. With a maximum 4 × 4 mm field of view and 7.4 μm axial resolution, the system offers reliable imaging capabilities. Noteworthy features include focal adjustability, rotary joint integration for fiber-twist-free operation, and a high-speed swept-source OCT laser at 200 kHz, facilitating real-time imaging. By providing insights into brain mechanisms and neurological disorders without disrupting natural behavior, this innovative system holds promise as a powerful tool in neuroscience research. Its compact design and comprehensive imaging capabilities make it well-suited for studying various brain regions and dynamic processes, contributing significantly to our understanding of brain function and pathology.
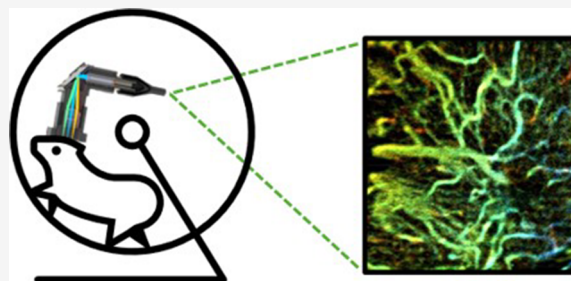
KEYWORDS: *swept-source OCT, Doppler OCT, OCTA, Alzheimer's disease, miniature OCT scope, brain image*

INTRODUCTION

Optical imaging has been widely used in neuroscience and health monitoring devices, especially noninvasive imaging modalities. Exploring the brain function mechanism is critical for developing new treatments and therapies for neurological disorders. For example, Alzheimer's disease (AD), an irreversible and incurable progressive neurodegenerative, poses an escalating threat to aging individuals. Other than the extracellular deposition of beta-amyloid plaques, and intracellular accumulation of neurofibrillary tangles that is commonly diagnosed by postmortem or cerebrospinal fluid analysis,[1−3] AD is also characterized by neuronal death, brain atrophy, and changes to the cerebral vasculature, such as reduced capillary density and changed capillary morphology,[4−7] which is suitable for applying the noninvasive imaging screening and diagnostics. However, many techniques require that the animal be immobilized or anesthetized, which can distort the data and limit the interpretation. For example, the behavior of an anesthetized animal may not accurately reflect how the brain responds to stimuli in a natural setting. Therefore, a miniaturized microscope is critical to visualize the structure and dynamic function of a free-moving animal brain with minimal effect on the animal's natural behavior.

In recent years, there has been considerable interest and effort in developing head-mounted optical imaging devices for use in freely moving mice. While notable studies such as photoacoustic microscopy have been conducted, they are limited by their axial resolution.[8] Techniques such as fluorescence imaging[9] and laser speckle imaging[10] lack depth information. Multiphoton fluorescence imaging (MPM) devices, including two-photon and three-photon microscopes, offer cellular-level spatial resolution and deeper penetration depth.[11,12] However, it has a limited field of view (FOV) of a few hundred micrometers and slow imaging speed, resulting in a lack of comprehensive tissue structure and vasculature information.

Optical coherence tomography (OCT), as a promising noninvasive technique that enables high-resolution cross-sectional imaging of biological tissue, has growing significance in brain imaging.[13] OCT offers micrometer-scale resolution, which is 10−100 times greater than other commercial imaging modalities, such as ultrasound, computed tomography (CT), and magnetic resonance imaging (MRI). Additionally, OCT provides a larger FOV of several millimeters, effectively overcoming the limitation of MPM. The extension of functional OCT imaging techniques, including OCT angiography (OCTA) and Doppler OCT (DOCT), represents a

significant improvement in brain vessel detection and analysis.[14−17] OCTA compares the decorrelation signal between sequential OCT b-scans taken at precisely the same cross-section to generate angiographic images without the need for intravenous dye administration.[18] DOCT has become an important in vivo blood vessel imaging method for its advantage of quantifying blood flow direction, as well as velocity with high sensitivity.[15−17,19]

Efforts were made to minimize the size of the OCT probe, especially endoscopic OCT for cardiovascular application. A common approach involved replacing the heavy collimator with a grin lens to reduce overall weight.[20] Additionally, a microelectromechanical systems (MEMS) device was employed for the laser scanning along with a separate control unit.[21] However, very few miniature probes were applied for OCT brain imaging. The only reported small scope for brain OCT on mice weighs 8 g, surpassing the 3 g weight limit necessary to preserve the natural activities of mice.[11,22] Another weight reduction method is fabricating with a lower density material, such as polyether ether ketone (PEEK) that was used for head-mount MPM scope in recent years.[11] PEEK is known for its exceptional strength-to-weight ratio, making it an ideal material for use in biomedical instruments. By integrating these features into our design, we developed a miniaturized head-mount OCT scope without compromising imaging speed and stability, enabling brain monitoring in freely moving, nontrained mice without disrupting their natural motion. This advancement allows for capturing vasculature changes during mice's self-determined actions.

In this paper, we report the first development of a miniaturized OCT scope with a weight of 1.5 g that can be mounted on a freely moving mouse head for brain OCT/OCTA imaging. In addition to weight reduction, the device's performance was enhanced in multiple aspects. First, it was designed as a focal-adjustable scope, allowing precise adjustment of the focal plane in awake mice and compatible with surgery procedures on different brain monitoring areas, thereby broadening its application. The system was also integrated with a rotary joint to provide a novel fiber-twist-free solution for facilitating long-term monitoring. The scope features a reliable, stable mounting design that is unaffected by mouse motion, critical for obtaining OCTA images. Moreover, the system is integrated with a high-speed swept-source OCT laser, enabling a scanning speed of 200 kHz and an axial resolution of 7.4 μm. Our customized program can visualize cross-sectional OCT images and Doppler phase changes that reflect blood flow in real time. Our fully assembled head-mount scope has a dimension as small as 15.5 mm × 11 mm × 8.5 mm and 1.5 g, providing a 4 × 4 mm field of view (FOV) that is optimized for visualizing the brain tissue through the standard 3 mm diameter surgery window of mice. The sensitivity of our system is 100 dB. Therefore, our functional head-mount OCT scope facilitates high-resolution, high-speed brain imaging in freely moving, freely behaving mice, which presents a critical advancement for a powerful tool to study the brain mechanism and neurological disorders, including AD.

METHODS

Animal Preparation. All experiments were managed according to the National Institutes of Health (NIH) guidelines for animal care and use and were authorized by the University of California, Irvine Institutional Animal Care and Use Committee (IACUC). To demonstrate the ability to

obtain stable OCT imaging in freely behaving mice, two male C57BL/6 mice, around 2−6 months old, were used in this study. Both mice were provided with free access to food and water in their home cages, with lighting maintained on a 12 h light/12 h dark cycle. One mouse underwent hippocampal CA1 cranial window surgery, and the other mouse underwent cortical cranial window surgery. For hippocampal CA1 imaging, the mouse was implanted with a cylindrical cannula on top of hippocampal CA1 as described in a previous publication.[23] Briefly, the cortical tissue and a thin layer of corpus callosum above mouse CA1 were carefully removed, and a cannula sealed with a glass coverslip at the bottom was implanted on top of CA1. For cortical cranial window surgery, the cortical tissue remained intact and was then covered with a glass coverslip without a cannula. Mouse received intramuscular dexamethasone injections before the surgery and subcutaneous carprofen daily for 3 days postsurgery. Around 3−4 weeks postsurgery, the mouse was fully recovered, and the hippocampus and the cortex were imaged via the OCT system. The imaging positions and angles were adjusted, and a baseplate was fixed on top of the cranial window as an adapter for the OCT scope.

Head-Mount Scope Design and System Setup. The miniaturized head-mounted DOCT scope, as shown in Figure 1, was designed using SolidWorks and manufactured with the
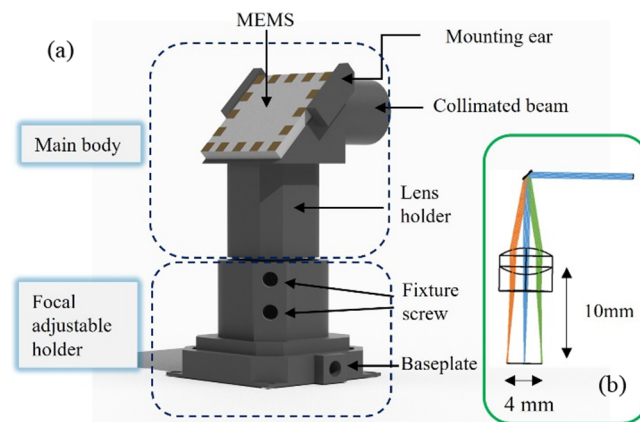

Figure 1. Design of the miniaturized head-mounted DOCT scope. The total weight of the assembled head-mount scope as shown is less than 1.5 g. (a) Main body and focal-adjustable holder. (b) Simulation of the MEMS mirror scan range and optical path using Zemax OpticStudio.

PEEK for lightweight purposes. The scope has two parts, the main body and a holder, to achieve the precise focal plane adjustment. The collimated beam from the grin-lens collimator is inserted into the cylinder structure of the main body. A 45-degree surface was specifically designed for mounting the MEMS mirror, allowing for vertical reflection and scanning at the sample plane. Two ear structures positioned at both sides of the MEMS surface serve as reference points for easy assembly. To optimize the clear aperture, the position of the 45-degree surface was carefully calculated, taking into account the depth difference between the mirror and the MEMS top surface. The scan lens is housed in a 5 mm inner diameter lens holder at the bottom of the main body, directing a focused beam to the target imaging area. Through careful dimensional analysis, the part ensures a clear aperture of no less than 4 mm. The holder, featuring a slightly larger dimension than the main

body, enables smooth insertion of the scope body. Two 0−80 screws are utilized to secure the main body firmly in place. Furthermore, the dimensions and shape of the holder bottom were tailored to be compatible with the baseplate used during the animal preparation process, ensuring seamless integration into experimental setups. Figure 1b is the Zemax OpticStudio simulation of the steering beam, showcasing a mechanical scan angle of ±5.6 degrees and achieving a maximum 4 mm scan range.

The OCT system utilizes a 200-kHz, 1310 nm center wavelength swept-source laser (SL132121, Thorlabs Inc.), as depicted in Figure 2a. A 90:10 fiber coupler splits the light into
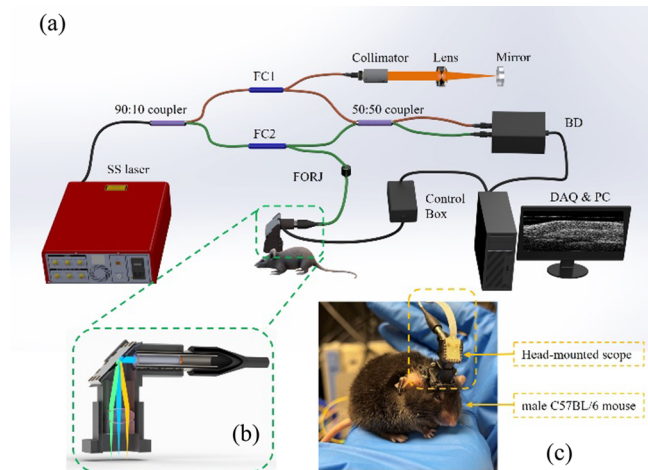

Figure 2. Schematic of the experiment system. (a) OCT system setup. The orange and green lines represent the optical path of the reference arm and sample arm, respectively. SS: swept source; BD: balance detector; FC: fiber circulator; FORJ: fiber optical rotary joint; PC: personal computer. (b) Illustration of the inner structure head-mounted scope. (c) Photo of the mouse that was mounted with the designed scope.

the sample arm and reference arm, with the majority directed to the sample. Two circulators are employed to separate the incident beam and back-reflected or backscattered signal. In the reference arm, the light passing through the circulator is collimated and focused using an appropriate lens. The beam reflected by the mirror is collected by the 50:50 coupler. In the sample arm, the light emerging from the circulator is collimated with a grin-lens collimator (50-1310A-APC, Thorlabs Inc.), which is affixed to the designed head-mount OCT scope. The laser scanning module incorporates a bare MEMS device (A7M20.2, Mirrorcle Tech) without an attached control board. The dual-axis MEMS integrates a 2 mm diameter aluminum-coated mirror and has a maximum mechanical scanning angle of ±5.6 degrees in each axis, corresponding to approximately 22 degrees optical scanning range in each axis. The resonant frequency of the MEMS is 1.3 kHz, meeting the requirement for fast scanning. The control signal is supplied through a surface-soldered flexible printed circuit and miniature insulated wires connecting to the MEMS driver via a homemade connector. To ensure a reliable and clear OCT image, the actual scanning pattern of the MEMS is crucial. Considering the MEMS mirror can be modeled as a second-order spring-mass system, the control signal must avoid exciting the resonant response that may induce oscillation and nonuniform scanning speed, despite the presence of an onboard fifth-order Bessel low-pass filter. In this system, the

input signal is optimized to achieve 2000 A-lines per frame, corresponding to a frame rate of 100 Hz. The light is focused by a 5 mm diameter, 10 mm focal length achromatic doublet lens with C-coating (AC-050-010-C, Thorlabs Inc.) and propagated to the desired sample area. The backscattered signal is transmitted to the 50:50 coupler, where it interferes with the reflected light from the reference arm at the balanced detector and is subsequently collected by the data acquisition system.

In Figure 2c, a photograph captures a mouse equipped with the designed scope. The lightweight nature of the scope enables the mouse to acclimate to the head-mounted scope within minutes without the need for additional training or exercise. During data acquisition, the mouse freely moves within its cage. The end fiber connecting to the scope extends 1m, providing ample mobility. A fiber optic rotary joint (FORJ) is utilized to mitigate torque forces resulting from fiber twists during free movement. Consequently, the assembled lightweight head-mounted DOCT scope enables DOCT imaging and brain monitoring in freely moving mice.

Image Processing. The principle of DOCT is the Doppler effect. The phase-resolved Doppler (PRD) technique extracts the Doppler frequency changes by calculating the phase difference between adjacent A-lines and is capable to quantify the blood flow direction and velocity.[17,24] However, the PRD image quality is highly dependent on the phase stability of the system. Considering that the phase instability may be caused by the movement of the freely moving mouse, we also employed the intensity-based Doppler variance (IBDV) method to reconstruct the angiography images of the moving mouse.[25] The technique was modified from the Doppler variance derived from the autocorrelation signal and averaging in both lateral and axial directions to increase the signal-to-noise ratio (SNR) and map the blood vessel based on the amplitude terms of the complex data.[26] The algorithm can be presented in the following equation:

$$\delta^2 = \frac{1}{T^2}\left[1 - \frac{\sum_{j=1}^{J}\sum_{n=1}^{N}\left(|A_{j,n}||A_{j+1,n}|\right)}{\sum_{j=1}^{J}\sum_{n=1}^{N}\frac{1}{2}\left(|A_{j,n}|^2 + |A_{j+1,n}|^2\right)}\right]$$

where δ^2 is the Doppler variance, $|A_{j,n}|$ is the amplitude of the complex data at the specific A-line and depth. J and N are the number of A-lines and depth positions that evolved for averaging. T is the time interval between adjacent A-lines.

Data Acquisition. To validate the system, we conducted in vivo imaging of a mouse undergoing hippocampal CA1 surgery. Multiple imaging sessions were carried out to assess the system's stability. Each frame comprised 2000 A-lines, and a total of 3000 B-scans were captured to reconstruct the entire hippocampal structure. Additionally, IBDV-based OCT angiography was performed on mice with a cortical cranial window surgery. Imaging sessions were conducted on both anesthetized and awake, freely moving mice to compare results and confirm the reliability of the scope when mounted on freely moving animals. Angiography data were generated from 1000 B-scan positions, with 2000 A-lines captured per B-scan. Our custom program facilitated the real-time visualization of the OCT/OCTA images.

■ RESULTS

Based on our prototype experience, we recognized the necessity of testing the scope's performance on a freely moving mouse rather than imaging a head-fixed, anesthetized mouse placed on a fixture. The mouse's movement posed a challenge for the scope's stability, especially when it encountered obstacles like walls. It was crucial to consider the mouse's spontaneous actions to verify the imaging capability effectively.

Figure 3a shows the OCT image of a cross-sectional hippocampus on a freely moving mouse obtained with the
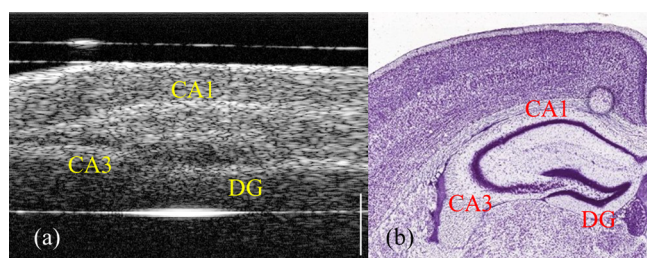

Figure 3. OCT image performance of the head-mount scope. (a) OCT image of the hippocampus CA1 on a freely moving mouse. (b) Anatomic reference of the mouse brain adapted from the Allen Mouse Brain Atlas, atlas.brain-map.org. Scale bar 1 mm.

head-mount scope. The CA1, CA3, and DG were marked on both the OCT image and the anatomic reference of the adult mouse brain that was adapted from the Allen Mouse Brain Atlas, as shown in Figure 3b. The high-resolution cross-sectional OCT image provides a clear visualization of the hippocampal structure, confirming the system's imaging ability. The imaging window, a 3 mm diameter cylindrical cannula, was entirely captured by our scope with a 4 mm × 4 mm field of view. The image presented in Figure 3 focuses on the hippocampus area while disregarding the tissue outside the cannula. The top layer indicates the cover glass reflecting the light, which can be adjusted to prevent washing-out scattered light signals from brain tissue. The CA1, CA3, and DG areas remained clearly distinguishable in the OCT image. The scale bar in the figure represents 1 mm, with the imaging range depicted as 2 mm. By combining OCT images from all B-scans, a three-dimensional structural image of the mouse brain can be obtained. The hippocampus tests conducted with the OCT head-mount scope on a freely moving mouse demonstrate comparable imaging performance to conventional OCT systems.

The DOCT angiography imaging was conducted on a mouse with cortical cranial window surgery. A video recording of freely moving mice is available in the Supporting Information. By collecting and analyzing the OCT complex data, as depicted in Figure 4a, the cross-sectional blood vessel image of each B-scan was acquired. The Doppler variance was calculated with B-scan cross-section OCT images of each position. The mouse freely moves in its cage during the data acquisition process. By combining these images and reslicing in the z-axis, which aligns with the optical path into the tissue, en-face angiography was obtained, as shown in Figure 4b. The volumetric OCTA images can be projected into two-dimensional images with depth-coding to present the blood vessels within a range. Figure 4c compares the angiography obtained with the head-mounted scope in both anesthetized and freely

moving mice. As well as the verification was with the bright-field image of the cortical cranial area after recovery from surgery. The DOCT angiography in Figure 4c was the projection of 400 μm depth. The colored arrows highlight the corresponding blood vessels in each figure. Three main blood vessels close to the surface were marked as the reference, within the photograph's clear imaging range. The scale bar in the figures remains at 1 mm, indicating an *en-face* angiography range of more than 2 mm in this experiment.

The projection angiography lacks directional information about the blood vessels. Therefore, a series of selected depth-resolved *en-face* Doppler variance images obtained with the IBDV algorithm are shown in Figure 5 for further illustration. Each image in Figure 5 represents a blood vessel projection image of a tissue slice of 40 μm. Blood vessels with smaller diameters emerge from a depth of 8 μm below the cover glass in Figure 5a, while larger-diameter blood vessels become more prominent as the imaging plane goes deeper in Figure 5h−l. The blood vessels at the bottom of the FOV become clearer from Figure 5h, which corresponds to a depth of 288−328 μm. The depth-resolved angiography obtained from imaging a freely moving mouse confirms the capability of capturing brain tissue blood vessels in a freely moving animal using our head-mount scope.

To further evaluate the stability of OCTA with the freely moving mouse, we calculated both the mean squared error (MSE) and structural similarity (SSIM). The MSE is the most traditional estimator to measure the similarity by calculating the average squared difference between two images pixel by pixel; however, it cannot capture the structural details. SSIM is an algorithm that incorporates perceptual information to evaluate the similarity between images, which take into account the luminance, contrast, and structure, thus more consistent with the human visual system's perception.[27] The mathematical expressions of MSE and SSIM are shown in the equations below:

$$\text{MSE} = \frac{1}{N} \sum_{i=1}^{N} (x_i - y_i)^2$$

where N is the total number of pixels, and x_i, y_i are the grayscale on each pixel of two images.

$$\text{SSIM} = [l(x, y)]^{\alpha}[c(x, y)]^{\beta}[s(x, y)]^{\gamma}$$

$$
\begin{cases}
l\left(x, y\right) = \dfrac{2\mu_x\mu_y + C_1}{\mu_x^2 + \mu_y^2 + C_1} \\[2mm]
c\left(x, y\right) = \dfrac{2\sigma_x\sigma_y + C_2}{\sigma_x^2 + \sigma_y^2 + C_2} \\[2mm]
s\left(x, y\right) = \dfrac{\sigma_{xy} + C_3}{\sigma_x + \sigma_y + C_3}
\end{cases}
$$

where $l(x, y)$, $c(x, y)$, and $s(x, y)$ represent luminance, contrast, and structure, respectively. μ_x and μ_y are the pixel sample mean, σ_x and σ_y are the standard deviations, σ_{xy} is the covariance of x and y, C_1, C_2, and C_3 are constants to stabilize the division, and α, β, and γ are positive numbers to adjust the weight, which typically equal to 1. The value of SSIM is between 0 and 1, and closer to 1 means a larger similarity. To
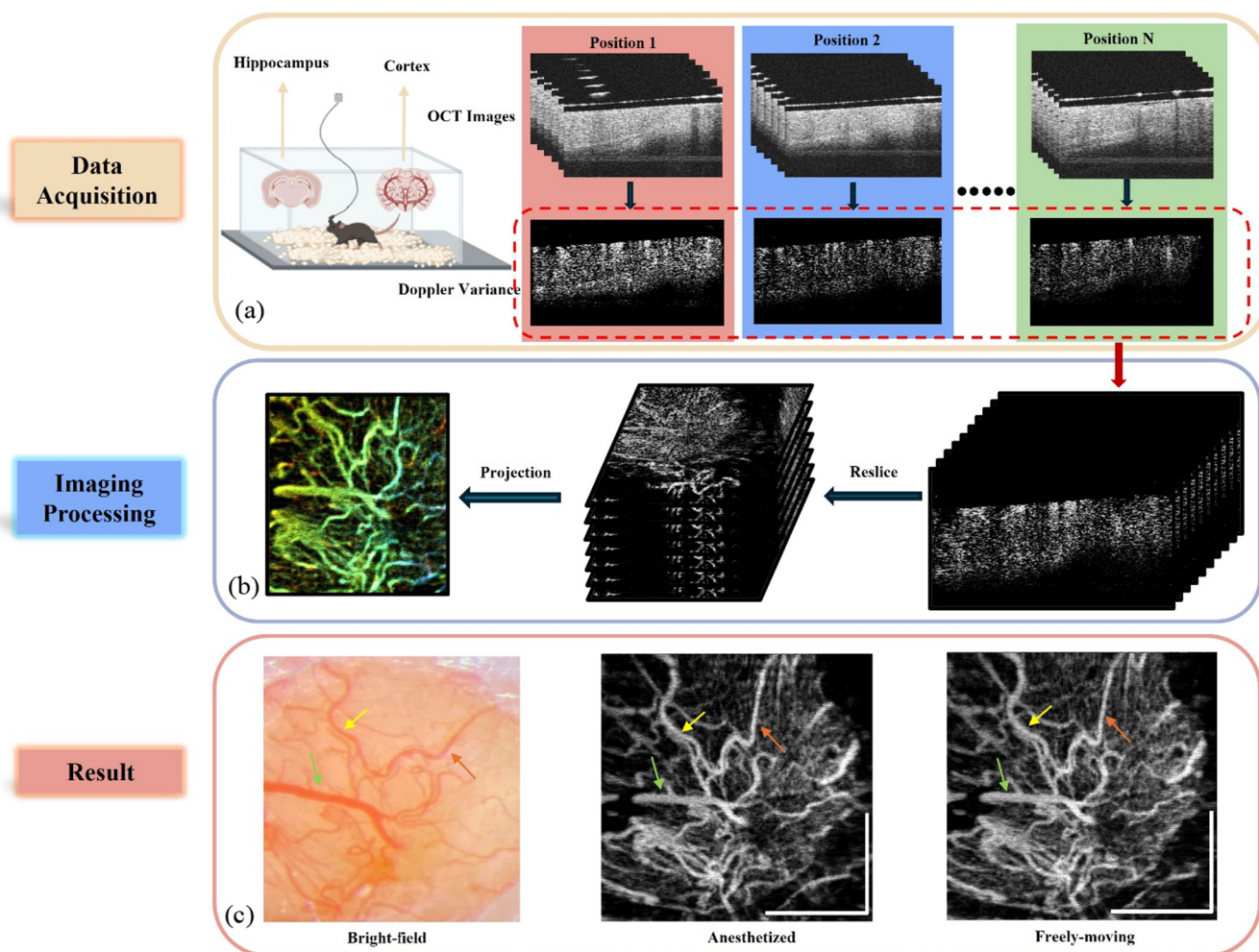
Figure 4. Imaging protocol, OCTA processing, and result. (a) Data acquisition block. The Doppler variance was calculated with B-scan cross-section OCT images of each position. The mice are freely moving in its cage during the data acquisition process. Created with BioRender.com (b) Reslice the Doppler variance along the *z*-axis to obtain the *en-face* OCTA images. Project the Volumatic image into a two-dimensional OCTA depth color-coded image. (c) Experiment result comparison. From left to right: the bright field of the imaging area; the angiography image under anesthetization; and the angiography image of freely moving mouse. Scale bar 1 mm.

ensure clarity and comparability, we calculate the normalized root MSE (NRMSE), which restricts the value range to [0,1]. A lower NRMSE indicates a greater similarity between two images.

We analyzed the similarity of OCTA images using 10 groups of data: five groups under anesthesia and five groups from freely moving mice, as shown in Figure 6. Figure 6a−c displays the MSE, NRMSE, and SSIM of six layers of depth-resolved OCTA images, respectively, while Figure 6d−f presents those of the volumetric angiography projection. In Figure 6a,b, the MSE/NRMSE under different conditions exhibits a similar trend, increasing with the probing depth. This is due to the blood vessel density being higher in deeper tissue, resulting in higher effective pixel intensity and larger MSE values. However, the NRMSE is consistently controlled under 0.03 for both conditions, indicating high repeatability. The SSIM, on the other hand, decreases as the depth increases. When blood vessels in deeper layers become clearer, those in upper layers may appear blurred due to being out-of-focus. This blurring of blood vessels decreases the SSIM. However, as shown in Figure 6c, the SSIM of both conditions remains acceptable within the range of [0.62, 0.82], with an average SSIM of 0.74.

Furthermore, we analyzed the similarity of the projection OCTA images to validate the stability of the system. The projection OCTA exhibits a more stable distribution compared to that of the layered images. Figure 6d,e shows the MSE and NRMSE of different conditions, and the cross-verification compares the five groups of freely moving data sets with a set of anesthetized data sets. The anesthetized data set is taken as the ground truth, and the similarity of the repeated imaging of freely moving mouse is calculated. This cross-verification is valuable in confirming the reliability of OCTA obtained from a freely moving mouse. The SSIM of the cross-verification demonstrates high repeatability, averaging around 0.86. These results affirm the stability of the designed scope for acquiring angiography images, which are susceptible to bulk motion during the movement of the imaging target.

By combining the 2D angiograph slices at different depths, a volumetric blood vessel structure can be easily generated. Figure 7 presents a color-coded OCTA image of the freely moving mouse cortex. In this image, the layer closer to the surface appears greener, while deeper layers exhibit a reddish hue, corresponding to an image depth of 428 μm. Color-coded depths enhance our ability to visualize blood flow dynamics within the brain tissue. Specifically, it allows for a clearer

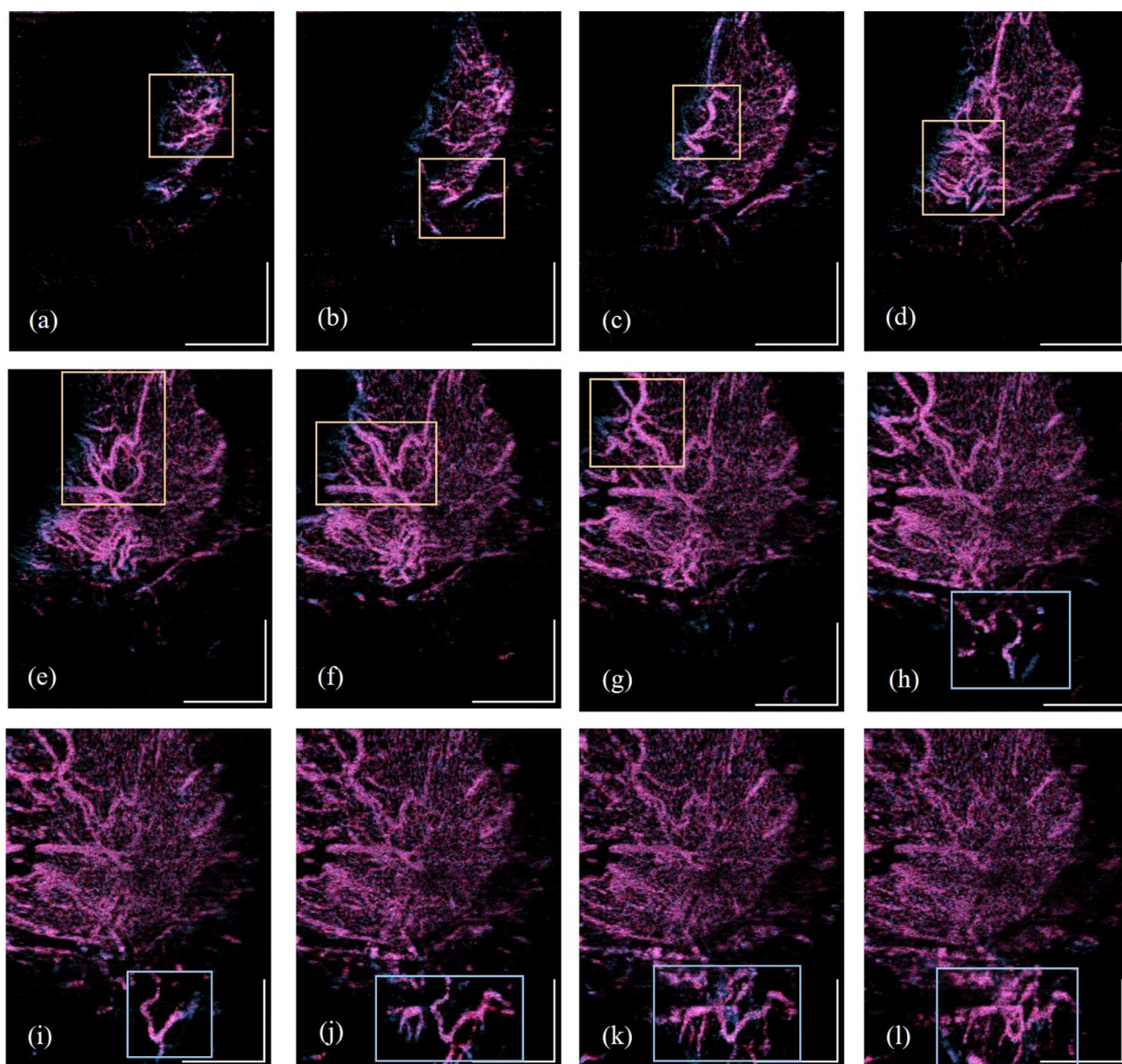**Figure 5.** Depth-resolved angiography of the mouse brain cortex of a freely moving mouse. Each angiography was the projection with a 40 μm slice. The corresponding image starting depths from (a−l) are 8, 48, 88, 128, 168, 208, 248, 288, 328, 368, 408, and 448 μm, respectively. The colored solid-line boxes mark the blood vessels at specific depths. (a−g) shows blood vessels that are mainly in the upper FOV. (h−l) shows that the blood vessels appear in the lower area. Scale bar 1 mm.

illustration of blood vessel directionality, facilitating more accurate tracing of blood vessels throughout the cortex. This color-coded OCTA image provides valuable insights into the vascular architecture and blood flow patterns within the mouse cortex, aiding in the study of brain function and neurovascular coupling in freely behaving animals.

The acquisition time for each angiography generating data set is less than 1 min, depending on the total number of B-scans. During the repeating experiments, there is no need to remove the head-mounted scope or disrupt the movement of the mice, thanks to its lightweight design. The mice quickly acclimate to the scope and resume movement in the cage, allowing for long-term brain monitoring.

■ DISCUSSION

The development of a miniaturized head-mounted DOCT scope represents a significant advancement in visualizing the functional dynamics of the brain in freely moving animals, offering a closer investigation into how the brain responds to natural and social behaviors. Designing such a scope posed several challenges, including weight, stability, and the ability to facilitate long-term monitoring. In this study, we successfully addressed these challenges by developing a miniaturized DOCT scope weighing only 1.5 g when fully assembled, ensuring stable imaging performance unaffected by the animal's self-determined actions. Our high-speed system boasts a 200 kHz A-line scanning speed and achieves a 7.4 μm axial resolution, enabling us to distinguish layered structures within the brain. This capability was demonstrated through imaging of the adult mouse hippocampus. To validate our system, we
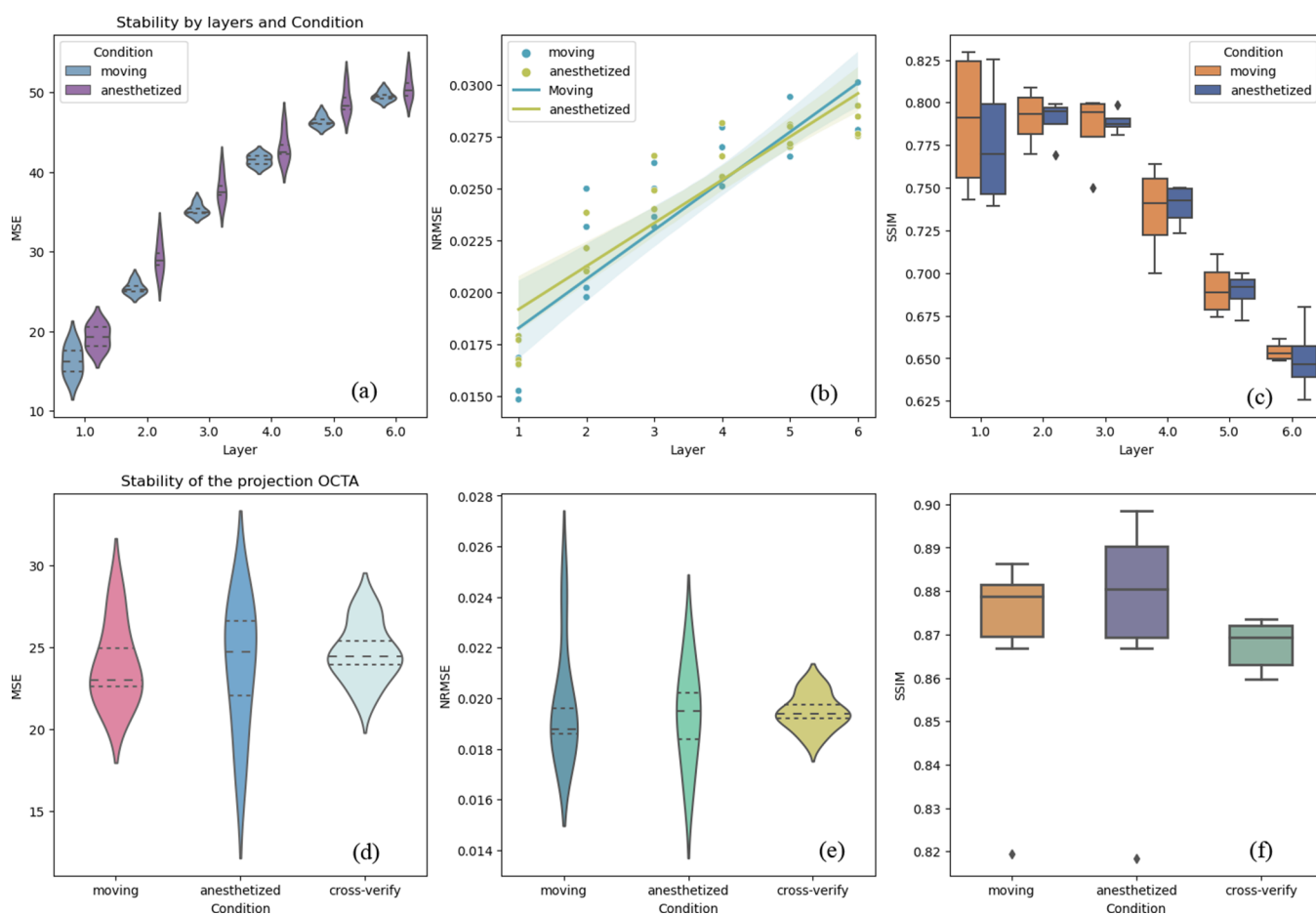
Figure 6. Analysis of the stability of reliability of the designed scope and system. (a−c) MSE, NRMSE, and SSIM of six layers of depth-resolved OCTA imaging. Both anesthetized and freely moving mouse data analyzed. (d−f) MSE, NRMSE, SSIM of the projection OCTA imaging within 480 μm depth. The imaging condition includes moving, anesthetized, and cross-verify, which involves taking a group of anesthetized imaging as ground truth and comparing the similarity of data obtained from a freely moving mouse.
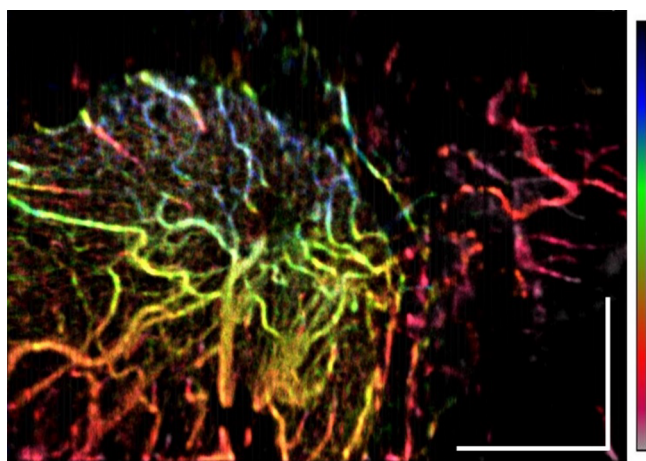

Figure 7. Projection view of the OCTA image for all layers in the freely moving mouse cortex with depth color-coded. Scale bar 1 mm.

compared OCTA images obtained from both anesthetized and freely moving mice. We incorporated a fiber optic rotary joint to facilitate long-term monitoring without the need to remove the scope, enhancing its usability in more biomedical studies.

Our system can visualize OCT/OCTA images in real time, underscoring its ability to visualize and monitor brain tissue for studying disease progression. The miniaturized DOCT scope

holds promise for integration with other imaging modalities, such as multiphoton imaging, to provide cellular-level information including neuron activities. Combining imaging modalities to capture tissue structure, blood vessel direction and flow speed, and neuron activity in freely moving mice can significantly advance our understanding of progressive neurodegenerative diseases like AD and aid in the development of new diagnostic tools.

■ ASSOCIATED CONTENT

Data Availability Statement

The data are available from the corresponding author upon reasonable request.

ⓈI Supporting Information

The Supporting Information is available free of charge at https://pubs.acs.org/doi/10.1021/acsphotonics.4c00856.

> Real-time OCT imaging alongside a freely moving mouse in a cage as mentioned in the text (MP4)

■ AUTHOR INFORMATION

Corresponding Author

Zhongping Chen − *Beckman Laser Institute and Department of Electrical Engineering and Computer Science, University of California Irvine, Irvine, California 92612, United States; Department of Biomedical Engineering, University of*

California Irvine, Irvine, California 92612, United States; orcid.org/0000-0002-4584-4560; Email: z2chen@uci.edu

Authors

Jingyi Wang − Beckman Laser Institute and Department of Electrical Engineering and Computer Science, University of California Irvine, Irvine, California 92612, United States; orcid.org/0000-0002-8722-2401

Qiao Ye − Department of Biomedical Engineering, University of California Irvine, Irvine, California 92612, United States; Department of Anatomy and Neurobiology, University of California Irvine, Irvine, California 92697, United States

Lidek Chou − Beckman Laser Institute, University of California Irvine, Irvine, California 92612, United States

Saijun Qiu − Beckman Laser Institute, University of California Irvine, Irvine, California 92612, United States; Department of Biomedical Engineering, University of California Irvine, Irvine, California 92612, United States

Xiangmin Xu − Department of Biomedical Engineering, University of California Irvine, Irvine, California 92612, United States; Department of Anatomy and Neurobiology, University of California Irvine, Irvine, California 92697, United States

Complete contact information is available at:
https://pubs.acs.org/10.1021/acsphotonics.4c00856

Author Contributions

Z.C. and J.W. conceived the project. J.W. designed the device hardware, system buildup and performed testing and characterization, and performed the data analysis. J.W. and Q.Y. conducted experiment and collected data. Q.Y. conducted surgeries and postoperative animal monitoring/care. L.C. fabricated the prototype and helped in data analysis. J.W. wrote the paper (with assistance from Q.Y.). S.Q. supported the original draft. All authors read and provided comments on the paper. Z.C. and X.X. supervised the work.

Notes

The authors declare no competing financial interest.

■ REFERENCES

(1) Bloom, G. S. Amyloid-β and tau: the trigger and bullet in Alzheimer disease pathogenesis. *JAMA Neurol* **2014**, *71* (4), 505−508.

(2) Javaid, F. Z.; Brenton, J.; Guo, L.; Cordeiro, M. F. Visual and Ocular Manifestations of Alzheimer's Disease and Their Use as Biomarkers for Diagnosis and Progression. *Front Neurol* **2016**, *7*, 55.

(3) Thal, L. J.; Kantarci, K.; Reiman, E. M.; Klunk, W. E.; Weiner, M. W.; Zetterberg, H.; Galasko, D.; Praticò, D.; Griffin, S.; Schenk, D.; et al. The role of biomarkers in clinical trials for Alzheimer disease. *Alzheimer Dis Assoc Disord* **2006**, *20* (1), 6−15.

(4) Arvanitakis, Z.; Capuano, A. W.; Leurgans, S. E.; Bennett, D. A.; Schneider, J. A. Relation of cerebral vessel disease to Alzheimer's disease dementia and cognitive function in elderly people: a cross-sectional study. *Lancet Neurol* **2016**, *15* (9), 934−943.

(5) Brown, W. R.; Thore, C. R. Review: cerebral microvascular pathology in ageing and neurodegeneration. *Neuropathol Appl Neurobiol* **2011**, *37* (1), 56−74.

(6) Smith, E. E.; Greenberg, S. M. Beta-amyloid, blood vessels, and brain function. *Stroke* **2009**, *40* (7), 2601−2606.

(7) Reitz, C.; Mayeux, R. Alzheimer disease: epidemiology, diagnostic criteria, risk factors and biomarkers. *Biochem. Pharmacol.* **2014**, *88* (4), 640−651.

(8) Guo, H.; Chen, Q.; Qin, W.; Qi, W.; Xi, L. Detachable head-mounted photoacoustic microscope in freely moving mice. *Opt. Lett.* **2021**, *46* (24), 6055−6058.

(9) Berdyyeva, T.; Otte, S.; Aluisio, L.; Ziv, Y.; Burns, L. D.; Dugovic, C.; Yun, S.; Ghosh, K. K.; Schnitzer, M. J.; Lovenberg, T.; et al. Zolpidem reduces hippocampal neuronal activity in freely behaving mice: a large scale calcium imaging study with miniaturized fluorescence microscope. *PLoS One* **2014**, *9* (11), No. e112068.

(10) Miao, P.; Lu, H.; Liu, Q.; Li, Y.; Tong, S. Laser speckle contrast imaging of cerebral blood flow in freely moving animals. *J. Biomed Opt* **2011**, *16* (9), No. 090502.

(11) Zong, W.; Obenhaus, H. A.; Skytøen, E. R.; Eneqvist, H.; de Jong, N. L.; Vale, R.; Jorge, M. R.; Moser, M. B.; Moser, E. I. Large-scale two-photon calcium imaging in freely moving mice. *Cell* **2022**, *185* (7), 1240−1256.e1230.

(12) Klioutchnikov, A.; Wallace, D. J.; Sawinski, J.; Voit, K. M.; Groemping, Y.; Kerr, J. N. D. A three-photon head-mounted microscope for imaging all layers of visual cortex in freely moving mice. *Nat. Methods* **2023**, *20* (4), 610−616.

(13) Huang, D.; Swanson, E. A.; Lin, C. P.; Schuman, J. S.; Stinson, W. G.; Chang, W.; Hee, M. R.; Flotte, T.; Gregory, K.; Puliafito, C. A. Optical coherence tomography. *Science* **1991**, *254* (5035), 1178−1181.

(14) Ren, H.; Ding, Z.; Zhao, Y.; Miao, J.; Nelson, J. S.; Chen, Z. Phase-resolved functional optical coherence tomography: simultaneous imaging of in situ tissue structure, blood flow velocity, standard deviation, birefringence, and Stokes vectors in human skin. *Opt. Lett.* **2002**, *27* (19), 1702−1704.

(15) Chen, Z.; Milner, T. E.; Dave, D.; Nelson, J. S. Optical Doppler tomographic imaging of fluid flow velocity in highly scattering media. *Opt. Lett.* **1997**, *22* (1), 64−66.

(16) Chen, Z.; Milner, T. E.; Srinivas, S.; Wang, X.; Malekafzali, A.; van Gemert, M. J.; Nelson, J. S. Noninvasive imaging of in vivo blood flow velocity using optical Doppler tomography. *Opt. Lett.* **1997**, *22* (14), 1119−1121.

(17) Zhao, Y.; Chen, Z.; Saxer, C.; Xiang, S.; de Boer, J. F.; Nelson, J. S. Phase-resolved optical coherence tomography and optical Doppler tomography for imaging blood flow in human skin with fast scanning speed and high velocity sensitivity. *Opt. Lett.* **2000**, *25* (2), 114−116.

(18) de Carlo, T. E.; Romano, A.; Waheed, N. K.; Duker, J. S. A review of optical coherence tomography angiography (OCTA). *Int. J. Retina Vitreous* **2015**, *1*, 5.

(19) Izatt, J. A.; Kulkarni, M. D.; Yazdanfar, S.; Barton, J. K.; Welch, A. J. In vivo bidirectional color Doppler flow imaging of picoliter blood volumes using optical coherence tomography. *Opt. Lett.* **1997**, *22* (18), 1439−1441.

(20) Xie, T.; Guo, S.; Chen, Z.; Mukai, D.; Brenner, M. GRIN lens rod based probe for endoscopic spectral domain optical coherence tomography with fast dynamic focus tracking. *Opt Express* **2006**, *14* (8), 3238−3246.

(21) Jung, W.; Zhang, J.; Wang, L.; Wilder-Smith, P.; Chen, Z.; McCormick, D. T.; Tien, N. C. Three-dimensional optical coherence tomography employing a 2-axis microelectromechanical scanning mirror. *IEEE J. Sel. Top. Quantum Electron.* **2005**, *11* (4), 806−810.

(22) Guo, X.; Li, X.; Wang, X.; Li, M.; Dai, X.; Kong, L.; Hao, Q.; Zhao, J.; Huang, Y.; Sun, L. Wearable optical coherence tomography angiography probe for freely moving mice. *Biomed Opt Express* **2023**, *14* (12), 6509−6520.

(23) Bouin, A.; Wu, G.; Koyuncu, O. O.; Ye, Q.; Kim, K. Y.; Wu, M. Y.; Tong, L.; Chen, L.; Phan, S.; Mackey, M. R.; et al. New rabies viral resources for multi-scale neural circuit mapping. *Mol. Psychiatry* **2024**.

(24) Vakoc, B.; Yun, S.; de Boer, J.; Tearney, G.; Bouma, B. Phase-resolved optical frequency domain imaging. *Opt Express* **2005**, *13* (14), 5483−5493.

(25) Liu, G.; Chou, L.; Jia, W.; Qi, W.; Choi, B.; Chen, Z. Intensity-based modified Doppler variance algorithm: application to phase instable and phase stable optical coherence tomography systems. *Opt Express* **2011**, *19* (12), 11429−11440.

(26) Liu, G.; Lin, A. J.; Tromberg, B. J.; Chen, Z. A comparison of Doppler optical coherence tomography methods. *Biomed Opt Express* **2012**, *3* (10), 2669−2680.

(27) Wang, Z.; Bovik, A. C.; Sheikh, H. R.; Simoncelli, E. P. Image quality assessment: from error visibility to structural similarity. *IEEE Trans Image Process* **2004**, *13* (4), 600−612.